Mapping Heterogeneity of Pristine and Aged Li- and Na-Mnhcf Cathode by Synchrotron-Based Energy-Dependent Full Field Transmission X-ray Microscopy

Mariam Maisuradze, Min Li, Angelo Mullaliu, Andrea Sorrentino, Dino Tonti,*
Stefano Passerini, and Marco Giorgetti*

Manganese hexacyanoferrate is a promising cathode material for lithium and sodium ion batteries, however, it suffers of capacity fading during the cycling process. To access the structural and functional characteristics at the nanometer scale, fresh and cycled electrodes are extracted and investigated by transmission soft X-ray microscopy, which allows chemical characterization with spatial resolution from position-dependent x-ray spectra at the Mn L-, Fe L- and N K-edges. Furthermore, soft X-rays prove to show superior sensitivity toward Fe, compare to hard X-rays. Inhomogeneities within the samples are identified, increasing in the aged electrodes, more dramatically in the Li-ion system, which explains the poorer cycle life as Li-ion cathode material. Local spectra, revealing different oxidation states over the sample with strong correlation between the Fe L-edge, Mn L-edge, and N K-edge, imply a coupling between redox centers and an electron delocalization over the host framework.

1. Introduction

Energy production as well as its storage is a complex and challenging task, especially when the demand is constantly increasing, therefore, the development of efficient energy storage devices is of an upmost importance. Batteries play a crucial role due to their ability to reversibly store and release energy when needed. Lithium-ion batteries (LIBs) are the fastest growing battery technology, which will soon be dominating the market of secondary batteries, because of their high energy density, high power density and long service life.[1] However, lithium is experiencing a dramatic price surge, caused by its limited supply and abundance, and uneven geographical distribution of Li and other critical raw materials, especially in the perspective of the large-scale automotive and grid storage markets. On the other hand, Na, which is one of the most promising post-Li technologies, has wide availability and low cost, as it is the 6th most abundant element in the Earth crust. Also, Na^+/Na redox couple with a reduction potential of -2.73 V versus standard hydrogen electrode (SHE), is close to Li^+/Li (-3.02 V vs SHE), making it a promising candidate by enabling similar operating voltages.[2,3] It has to be considered that Na has a higher molar mass and larger ionic radius compared to Li (1.02 Å for Na^+ vs 0.76 Å for Li^+), leading to differences in chemical and electrochemical properties.[4] Higher chemical reactivity of Na can cause rapid electrolyte consumption and faster solid electrolyte interphase formation.[5–8] On the other hand, Na does not form an alloy with Al, even at reduced potentials, therefore Al can be used instead of Cu as the current collector, further reducing the price of sodium-ion batteries (SIBs).

M. Maisuradze, M. Li, M. Giorgetti
Department of Industrial Chemistry "Toso Montanari"
University of Bologna
Viale del Risorgimento 4, Bologna 40136, Italy
E-mail: marco.giorgetti@unibo.it
A. Mullaliu, S. Passerini
Helmholtz Institute Ulm (HIU)
Helmholtzstrasse 11, 89081 Ulm, Germany

A. Mullaliu, S. Passerini
Karlsruhe Institute of Technology (KIT)
P.O. Box 3640, 76021 Karlsruhe, Germany
A. Sorrentino
ALBA Synchrotron Light Source
Carrer de la Llum 2–26, Cerdanyola del Vallés 08290, Spain
D. Tonti
Institut de Ciència de Materials de Barcelona
Consejo Superior de Investigaciones Científicas (ICMAB-CSIC)
Campus UAB Bellaterra, Cerdanyola del Vallès 08193, Spain
E-mail: dino.t@csic.es
S. Passerini
Department of Chemistry
Sapienza University of Rome
P.le A. Moro 5, Rome 00185, Italy

The use of Al as the negative current collector also enables full discharge of the cells (100% depth of discharge, DOD) making the storage and shipment much safer.

During the cycling of the battery, the positive (cathodic) and the negative (anodic) electrode materials undergo reversible redox reactions, implying the uptake or release of the ions to maintain electroneutrality. Thus, cathodic and anodic electrode materials should allow the rapid uptake and release of the ions with the lowest possible lattice strain.[9] This should be considered, together with all the fundamental differences between Li and Na to develop suitable, abundant, safe, and environmentally friendly electrode materials for SIBs.[4] The first attempts for the development of SIBs occurred in 1980, when TiS_2 was used as the host structure for the reversible Na^+ insertion/extraction process.[10] Layered oxide materials with the formula of A_xMO_2, where A and M are alkali ion and transition metal (TM), respectively, came as a later option for cathode materials.[11] Polyanions are also an important class of electrode materials for SIBs,[12–20] as are Prussian Blue Analogues (PBAs). These latter materials were introduced in 1980s and 1990s, but their application in non-aqueous electrolyte system for SIBs was first demonstrated in 2012.[21,22] From the PBA family is Prussian White, the cathode material of the first commercialized Na-ion batteries by Contemporary Amperex Technology Co., Ltd.[23] Prototypes based on PBAs are also developed in Sweden[24] and USA.[25]

PBAs are a large family of transition metal hexacyanoferrates with the general formula of $A_xM[Fe(CN)_6]_\gamma \square_{1-\gamma} \bullet zH_2O$, where A is an alkali metal such as Li^+, Na^+, K^+, etc.; M is a TM ion: Fe, Co, Mn, Ni, Cu etc.; γ is a vacancy; $0<x<2$; $0<y<1$.[26] PBAs have an open framework structure, redox-active sites and strong structural stability, together with being safe and relatively inexpensive. Because of the large ionic sites, they can reversibly accommodate and easily transport large cations. Generally, both redox centers of PBAs can be electroactive: $M^{+2/+3}$ (+1 to +2, for Cu, and +2 to +4 for Ni, respectively), and $Fe^{+2/+3}$, which means two electron redox capacity per molecular unit.[26] Due to their robust and large 3D channel frameworks, they are structurally and dimensionally stable, with almost zero lattice strain.[27]

Manganese hexacyanoferrate (MnHCF) is a PBA material displaying a high specific capacity and redox plateaus at a high voltage against both Li and Na in LIBs and SIBs,[28] but suffers significant capacity fading.[29] One of the possible causes affecting the lifetime of the battery is the inhomogeneous distribution of the oxidation state of the metal-sites inside the active material.[30] In the present study the electronic structure and possible heterogeneity of Li- and Na-(de)intercalated MnHCF, was analyzed by synchrotron-based energy-dependent full field transmission X-ray microscopy (TXM) in the soft X-ray range. This material has been already characterized by X-ray absorption spectroscopy (XAS)[28] in hard X-ray range and by X-ray diffraction (XRD).[31] TXM can provide a picture of the chemical state and spatial distribution of the elements inside the material, with resolution of few tens of nanometers. Moving the energy across the edge of interest while acquiring images, a whole XAS can be extracted at each image pixel. In previous studies, soft-TXM has already been successfully used in post-mortem studies for the identification of chemical heterogeneities in Li-rich, Co poor Mn oxide cathodes.[32] By using X-rays of the soft energy region (<3 KeV), it is possible to access transitions from core levels of light elements,

such as the K-edge of N, O, F, as well as L-edge and M- edge of heavier elements.[33] XAS in the hard X-ray range is widely used, as it is able to provide valuable information: the edge energy can be indicative of the oxidation state of the element, extended X-ray absorption fine structure (EXAFS) is sensitive to the geometric structure around the photo-absorber, and pre-edge shape is particularly informative about the metal coordination number and symmetry, as they are arising from the $1s \rightarrow 3d$ transitions, and 3d states contain information about the crystal fields, valences, chemical bonds, orbital, and spin characters of the material. Nevertheless, the hard-XAS is still limited, as pre-edge transitions are dipole-forbidden and quadrupole-allowed, and therefore, have a low intensity. Instead, by moving to the soft X-ray region, in sXAS (soft X-ray absorption spectroscopy), more intense $2p \rightarrow 3d$ dipole-allowed transitions can be accessed. Also, substantial increase in energy resolution is obtained, as deeper core-holes are filled faster, consequently, 1s core-hole lifetime is shorter than 2p, and because of the time-energy uncertainty relation the energy resolution for 3d metals increases from > 1 eV for K-edge to < 0.5 eV for L-edge.[34] Although, the necessity of performing the measurement in vacuum can be a limitation, especially for operando tests. For MnHCF, hard-XAS gives information about the local structure, especially for Mn: strong modification in local coordination of Mn (see details below), makes the differences in spectra between the charge states well-distinguishable. However, for Fe the oxidation state variation is much harder to identify.[28]

Specifically for this study, the use of TXM on MnHCF aimed to clarify the fade mechanism by analyzing the evolution of the spatial distribution of the Mn, Fe and N oxidation state in the active material upon the long-term cycling. The formation of domains affected by incomplete reaction was revealed.

2. Results and Discussion

2.1. Electrochemical Profiles

For the TXM experiment pristine, charged and discharged samples, after one (Li/NaC01; Li/NaD01) and fifty cycles (Li/NaC50; Li/NaD50) were prepared (summarized in Table S1, Supporting Information). In MnHCF, the electrochemical alkali ion release takes place during the charge process, while the insertion occurs during the discharge. The potential profiles of Li- and Na-cells (Figure S1, Supporting Information) are different because of the difference in terms of possible ion intercalation sites. The material is vacuum dried, which means the absence of adsorbed water, therefore during the positive polarization, desodiation occurs in a single extraction process (see Equation 1).[35,36] Even though there is still interstitial water inside the structure, following insertion for Na-ion system, as it is visible in **Figure 1**a, is again a single-step process, and polarization is very low, suggesting Na^+ from the electrolyte to occupy almost the same sites previously occupied by Na coming from the synthesis process. A plateau is observed at around 3.45 V (see Equation 2, Figure 1a,c). However, for the Li-ion insertion process, there is a competition not only between Li^+ and interstitial water, but also with Na^+ from the original synthesis, which is possibly the main reason for the multiple step insertion, that takes place at two different potentials, at ≈3.6 and 3.45 V. The second plateau is not well defined (see Equation 3, Figure 1b,d), and therefore higher slope is
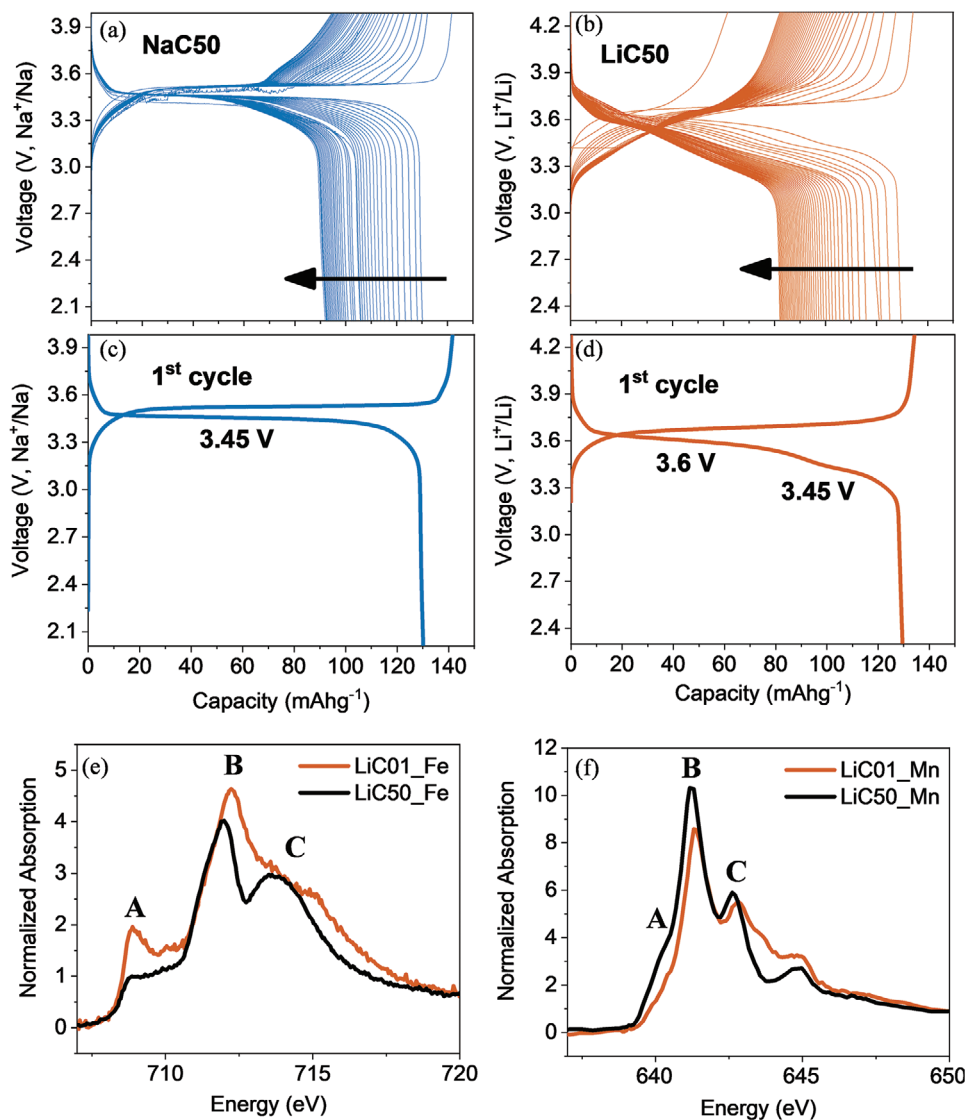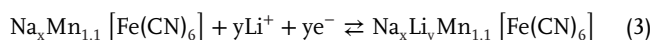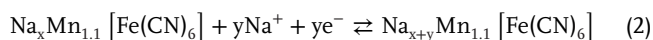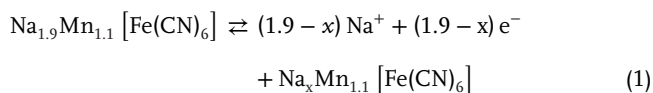
Figure 1. Galvanostatic charge/discharge of a) NaD01, b) LiD01, c) NaC50, and d) LiC50, and spectra of averaged signal from all the sample pixels in the field of view of e) LiC01 versus LiC50, and f) Mn L-edge LiC01 versus LiC50.

observed. As the system equilibrates in the following ion insertion steps the second plateau is getting weaker and transition to a single step insertion process is observed for Li-ions the same way as for Na-ions (Figure 1d; Figure S2, Supporting Information).

$$Na_{1.9}Mn_{1.1}\left[Fe(CN)_6\right] \rightleftarrows (1.9-x)\,Na^+ + (1.9-x)\,e^-$$
$$+ Na_xMn_{1.1}\left[Fe(CN)_6\right] \quad (1)$$

$$Na_xMn_{1.1}\left[Fe(CN)_6\right] + yNa^+ + ye^- \rightleftarrows Na_{x+y}Mn_{1.1}\left[Fe(CN)_6\right] \quad (2)$$

$$Na_xMn_{1.1}\left[Fe(CN)_6\right] + yLi^+ + ye^- \rightleftarrows Na_xLi_yMn_{1.1}\left[Fe(CN)_6\right] \quad (3)$$

2.2. Identification of the Transitions

In PBAs, sXAS is widely implemented as a site-sensitive probe of the TM redox centers,[37] as the N-coordinated and C-coordinated

TM ions are known for being in different spin states.[36] Due to the ligand, the C-coordinated ion experiences a large crystal field splitting, as C is σ-donor and π-acceptor, and therefore favors a low-spin (LS) state, whereas the N-coordinated ion as N is σ-donor, experiences a much lower crystal field splitting, which leads to a high-spin (HS) state,[38] both of them having the octahedral environment (Figure S3a,b, Supporting Information).[39] **Figure 2** displays the normalized Fe and Mn L-edge XAS for each state of charge, obtained as the averaged signal from all the sample pixels in the field of view.

In the Fe L-edge, three main transitions are observed (Figure 2a-d): Peak A at ≈709 eV, $2p \rightarrow 3d\ t_{2g}$, is only visible for Fe^{III}. Peak B, the most intense signal, occurs at ≈712 eV, corresponding to the transition $2p \rightarrow 3d\ e_g$, for both Fe^{III} and Fe^{II}: Fe^{III} LS $3d^5$ ($t_{2g}^5 + e_g^0$) and Fe^{II} LS $3d^6$ ($t_{2g}^6 + e_g^0$). Finally, Peak C, characteristic to the π-backdonation $2p \rightarrow \pi*(CN)-3d$ (metal with t_{2g} symmetry), appears ≈714 eV and is also visible for both

2300718 (3 of 11)

**ADVANCED
SCIENCE NEWS**

www.advancedsciencenews.com
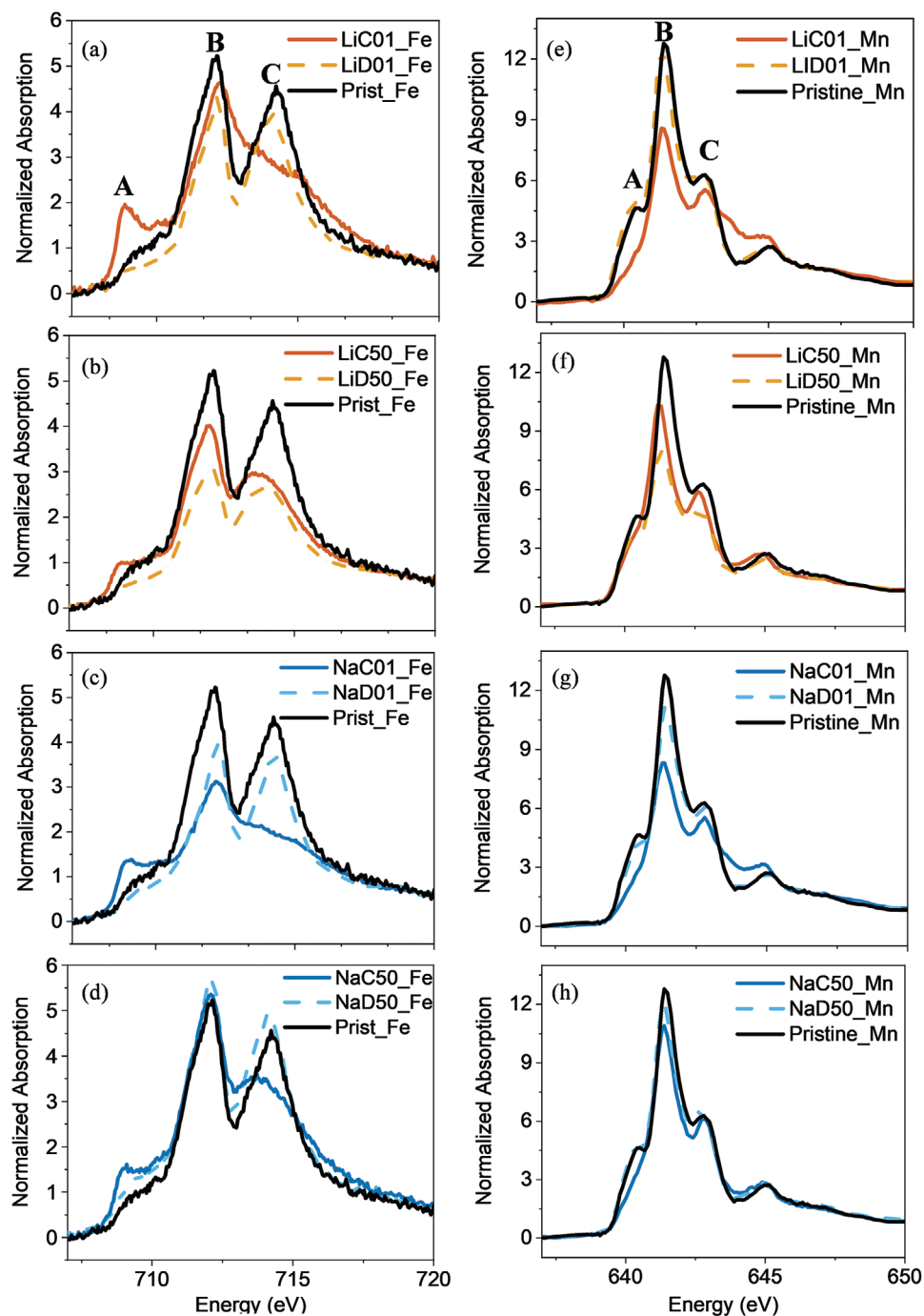
**small
methods**

www.small-methods.com

Figure 2. Spectra of Fe L-edge of averaged signal from all the sample pixels in the field of view of Li-containing sample (a,b), Na-containing sample (c,d), and Mn L-edge of Li-containing sample (e,f), and Na-containing sample (g,h). In each plot the corresponding Pristine spectrum is reported for comparison.

Fe^{III} and Fe^{II}, but back-donation is generally stronger in case of Fe^{II} (Figure S3d, Supporting Information). The same transitions from $2p_{1/2}$ (L_2 edge) are visible at higher energy (725–727 eV).[40] So, when Fe^{II} LS is oxidized to Fe^{III} LS, the main change in the corresponding spectra is a peak at lower energy consisting of the Fe t_{2g} orbital. Therefore, the reversible redox reaction during ion

insertion/extraction process occurs mainly on the t_{2g} orbital of Fe (Figure S3b, Supporting Information).[41]

Generally, also for the Mn L-edge, three peaks are visible (Figure 2e-h): Peak A transition just above 640 eV is appearing only in discharged samples for Mn^{II}, $3d^5$ ($t_{2g}^3 + e_g^2$) and is not any longer visible after the oxidation (Mn^{III}, $3d^4$ ($t_{2g}^3 + e_g^1$)); the

**ADVANCED
SCIENCE NEWS**

www.advancedsciencenews.com
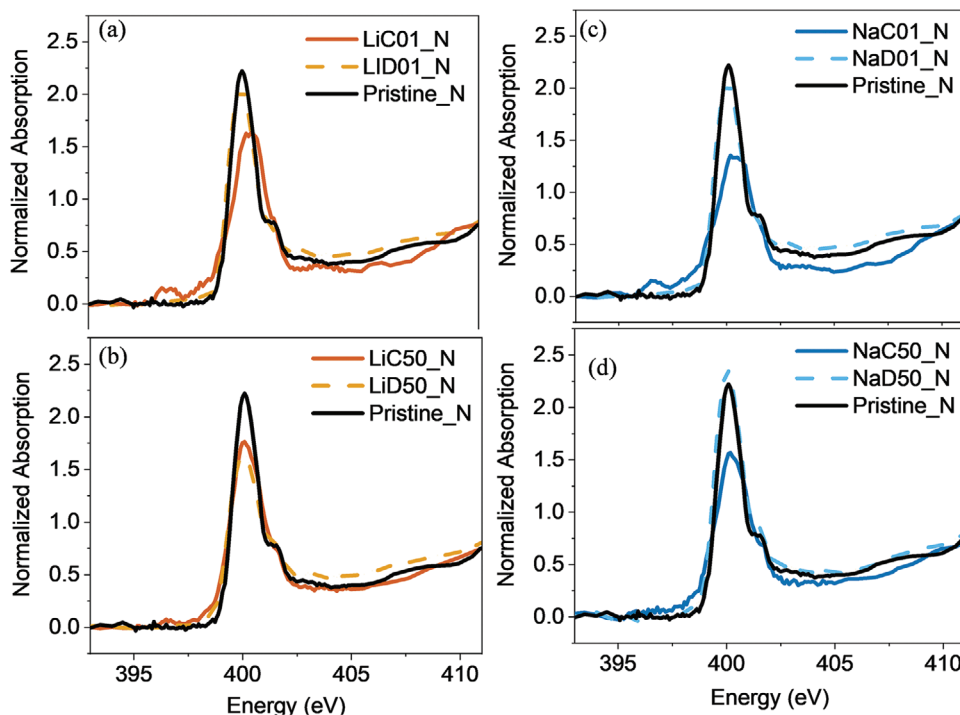
**small
methods**

www.small-methods.com

Figure 3. Spectra of N K-edge of averaged signal from all the sample pixels in the field of view of Li-containing sample (a,b) and Na-containing sample (c,d).

most intense peak is Peak B at 641 eV, followed by Peak C at ≈642–643 eV.

There is a strong interaction and consequently a charge-transfer transition between the Mn t_{2g}, Fe t_{2g}, and CN π* orbitals.[42–44] Asakura et al. suggested that there might be a class II mixed-valence state, which means moderate electronic coupling between the redox centers with partially localized charges,[45] here with electron delocalization over the entire framework of MnFe-PBA. In their study they performed Fe $L_{2,3}$-edge ($2p_{1/2,3/2} \rightarrow 3d$ absorption) XAS for $K_3[Fe^{II}(CN)_6]$ and $K_4[Fe^{III}(CN)_6]$, together with charge-transfer multiplet (CTM) calculations, clarifying the Fe oxidation state and the degrees of donation and back-donation between Fe and the cyanide ligand.[41] In the CTM calculations, according to Hocking et al.,[43] the Fe L-edge spectra of $[Fe^{III}(CN)_6]^{3-}$ and $[Fe^{II}(CN)_6]^{4-}$ could be explained only when the metal-to-ligand charge transfer (MLCT) (π back donation) and the ligand-to-metal charge transfer (LMCT) (π/σ back donation) are taken into account.

Unfortunately, multiplet calculations are less precise for Mn^{III} sXAS spectra and are further complicated by the near degeneracy of Mn and Fe electron acceptor states.[41] In addition Mn^{III} compounds are Jahn-Teller (JT) active. During the oxidation the removal of one electron occurs from the e_g orbital of d^5 Mn^{2+} HS,[21] but JT effect leads to the basal plane shrinkage (Figure S3c, Supporting Information[28]), and different orbital distribution, being the d_{z^2} less perturbed by the potential generated by the cyanides, than the $d_{x^2-y^2}$ (Figure S3c, Supporting Information).[46] The abovementioned hurdles make very difficult to assess the precise Mn oxidation state from multiplet calculations when the electrode is fully charged.[38] However, the in-

creased the spectral weight on the high photon energy side suggests the presence of high state of charge.[47]

It is important to notice that changes of the state of charge are more straightforward to detect for Fe than Mn, giving complementary information to the metals' K-edge investigation by hard X-rays, where Mn is highly concerned but only little changes are observed for the Fe site.[28] However, the results from both soft and hard X-rays for MnHCF characterization, clearly indicate that the charge compensation involves both the Fe and Mn centers.

The average spectra of Mn and Fe L-edges here reflect the results obtained from the galvanostatic charge/discharge (GCD) of the corresponding samples. (Figure 1e,f; Figure S3, Supporting Information). In the aged electrodes GCD shows the decrease of the capacity, and consequently in the corresponding spectra characteristic spectral features become less evident. Furthermore, features characteristic to the oxidized material appear in the discharged electrodes and vice versa. In the Fe L-edge spectra of LiC50, peak A intensity is decreased and peak C has more a defined shape than just a shoulder (Figure 1e). Similarly to the Fe L-edge, in the Mn L-edge, the spectral weight of LiC50 electrode at high energy (peak C and above), characteristic to the oxidized Mn, is decreasing during the cycling of the electrode (Figure 1f). Same observation is true for Na samples and for the aged discharged electrodes (Figure S5, Supporting Information). This phenomenon strongly suggests that upon cycling the cation uptake and release is, on average, incomplete both in fully discharged and fully charged electrodes.

The XAS N K-edge shows only a slight change with ion extraction (**Figure 3**): the main peak assigned to the π* orbital of hybridized CN^- at 400 eV[45] is shifted toward higher energy, and

**ADVANCED
SCIENCE NEWS**

www.advancedsciencenews.com

**small
methods**

www.small-methods.com

decreased in intensity upon charging. The peak is wide, especially in C01 samples, which might suggest two different contributions of N. The reason behind this phenomenon can be explained by diverse local environment of N. As mentioned above, the JT activity leads to the different orbital contribution for Mn^{3+}, and therefore the distance between axial and equatorial Mn—N bonds is not the same anymore, namely, the equatorial one is shrinking from 2.18 Å → 1.96 Å.[28] After cycling the shape of the N peak at 400 eV was more retained in the NaC50 electrode than in LiC50. As the spectra represent an average of whole samples, and there is a strong interaction between Mn t_{2g}, Fe t_{2g}, and CN π^*, this behavior suggests the higher decrease of both total Fe^{III} and Mn^{III} content in LiC50, than in NaC50 (compared to the corresponding C01s) in agreement with the evolution of Fe and Mn spectra (Figure 2). Another difference in the N K-edge spectra during ion extraction is the appearance of the small peak at 397.3 eV, which could be associated to the π orbital hybridized with the Fe t_{2g} orbital.[44] This hybridization state disappears due to the electron filling,[48] when Fe^{III} LS $3d^5$ ($t_{2g}^5 + e_g^0$) is reduced to Fe^{II} LS $3d^6$ ($t_{2g}^6 + e_g^0$). However, this peak is clearly visible only in the C01 samples and is poorly retained after aging, which might again suggest the decrease of the total Fe^{III} content inside the material. Since in the charged samples oxidized forms of Fe and Mn should exist, the decreased concentration of 3+ metals can be ascribed to the reduced cell performance. Concerning the discharged samples, NaD50 had almost identical spectral features as NaD01, whereas the peak intensity in the LiD50 has dropped the same way as of the corresponding charged samples, which suggests the partial retention of Fe^{III} in LiD50 (Figure 3b).

2.3. Spatial Inhomogeneities

To understand the development of incomplete average intercalation/deintercalation upon cycling, it is useful to inspect the spatial distribution of the state of charge in the active material of the electrode. To demonstrate the local variation of two components in the actual sample, the arctangent of the ratio between peak A and C is represented (**Figure 4**). Based on the assignment discussed in the previous section, this parameter qualitatively represents the degree of oxidation, with high values indicating more oxidized Fe and more reduced Mn. Thus, these images highlight certain regions within the sample where the oxidation state deviates from the average. It is evident that the active particles are not homogeneous within the resolution of ≈40 nm. Sometimes the part of the dots cloud which deviate from the main pattern can be attributed to a specific zone of the sample, as it is shown in Figure S6b (Supporting Information), for the Mn L- edge of the.

The plots in Figure 4b,d show that inhomogeneities are present in all samples, even in pristine (Figures S7 and S8, Supporting Information), but are particularly evident in the cycled samples. The corresponding images (Figure 4a,c) also agree with this observation.

The heterogeneities are more visible in the Fe L-edge compared to the Mn one in the aged electrodes (Figure 4e,f). The histograms of the chemical state maps, on which x axis is A versus C balance, which corresponds to the arctangent ratio between peak A and C, and therefore it shows the same intensity as chemical state maps, and y axis is count of pixels on given x, represent the

distribution of oxidation state over the whole field of view, and prove that the range of the intensity is broader in case of Fe L-edge (Figure 4g), again highlighting the fact that the sensitivity is higher for Fe L-edge, than for the Mn one.

In the cycled samples not only spatial inhomogeneities are more evident, but the spectral deviations from the average spectra also increase. For a closer investigation the charged cycled samples (LiC50 and NaC50) were chosen (**Figure 5**). Most parts of the C50 on the Fe L-edge are quite similar to the C01, but others rather show similarities to the reduced sample. In case of both Fe_LiC50 and Fe_NaC50 (Figure 5e,a) most selections (Figures S11 and S15, Supporting Information), which were chosen as described in the experimental part, such as Fe_NaC50_S1 and Fe_LiC50_S2 (Figure 5b,f) are more or less typical of the oxidized sample, with higher Peak A/Peak C ratio. Instead, most reduced regions (in blue, Figure 5c,g) present more similarities to the D01 sample (details will follow below). For these regions, while peak A still shows a shoulder in both NaC50 and LiC50 (as generally expected in charged samples), similarity with the discharged samples are mainly evident around peak C region, which has higher intensity in the Li-containing sample (Figure 5d,h). Larger deviation from the expected spectra for the Li-ion system indicates a more pronounced degradation that correlates well with the larger capacity fading of the LiC50 sample in comparison with NaC50 (Figure 1c,d). More oxidized/reduced regions have random distribution throughout smaller particles as well as bigger aggregates.

Typically, deviating regions were observed at the same locations in the Mn L-edge as in Fe. For example, as shown in Figure 5i–l the difference between Fe_LiC50_S2 and Fe_LiC50_S6 are reflected in Mn spectra, with differences in intensity of peak A region and spectral weight distribution on the high energy region.

To assess if purely intercalated or deintercalated domains can be resolved in the cycled samples, in **Figure 6** the selection of most oxidized and most reduced parts of LiC50 are compared to LiC01 and LiD01, respectively. In Fe_LiC50_S2 (Figure 6a) the Peak A region is quite comparable to the first charged sample; however Peak C is still a distinct peak rather than a shoulder. Similarly, in Mn_LiC50_S2 (Figure 6b), the spectral weight distribution on the high energy side is quite comparable to Mn_LiC01, but still a shoulder at Peak A region is present. This means that not even the most oxidized regions of the cycled sample fit the average spectra found at the first oxidation, suggesting significant amounts of intercalated Li that cannot be spatially resolved. The most reduced region Fe_LiC50_S6 is compared to Fe_LiD01 in Figure 6c. Also in this case, full overlap is not observed – Peak A is still visible as a shoulder and Peak B/Peak C ratio never goes ≈1. We conclude, that despite some similarities, this domain is not as reduced as the typical discharged sample. The same is true for Mn_LiC50_S6, although two spectra are very close to each other (Figure 6d), Peak A is still less defined than in Mn_LiD01. The presence of such regions inside the sample can be attributed to fragments that have been electrically disconnected. This disconnection and deactivation of some particles, may be due to the anisotropic volume change, which can lead to the stress or strain inside the structure.[30,49] Indeed, from the pristine electrode to the charged one, as Mn oxidation state increases from +2 to +3 and basal shrinkage occurs, the Mn-N distance reduces by 10% (as already discussed above).[28]
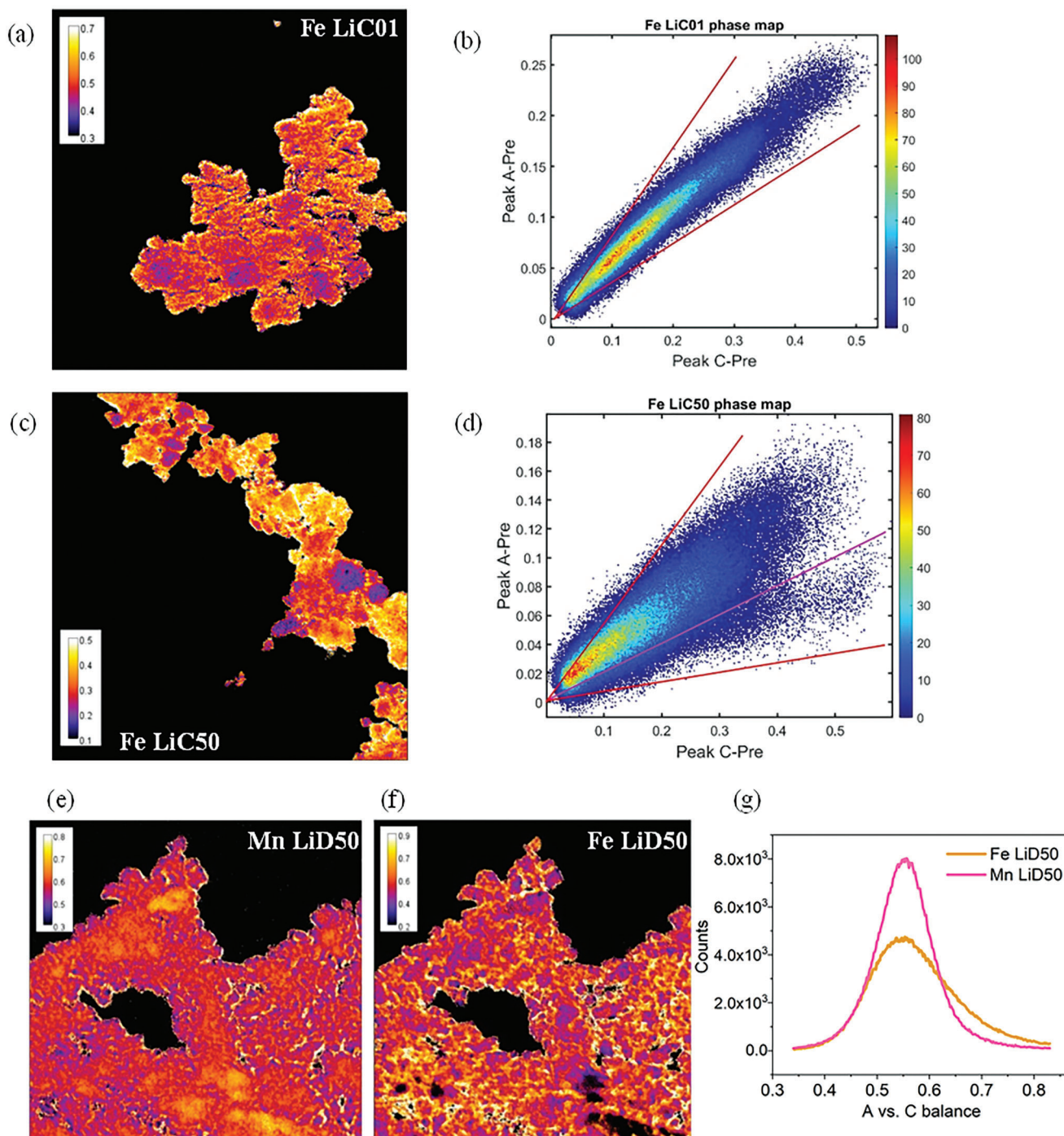
ADVANCED
SCIENCE NEWS
www.advancedsciencenews.com

small
methods
www.small-methods.com

Figure 4. Chemical state maps and corresponding scatter plots of a,b) Fe L-edge of LiC01 and c,d) LiC50; chemical state map of LiD50: e) Mn L-edge, f) Fe L-edge, and g) corresponding histograms, where A versus C balance corresponds to arctangent ratio between peak A and C.

The better homogeneity of the sample cycled in Na⁺ is also demonstrated by the histograms of the chemical state maps for the whole set of data, as a semi-quantitative comparison of heterogeneity between different samples as shown in **Figure 7**. On both Fe and Mn L images, with the only exception of D50 (Fe) and D01 (Mn), the Na sample always look more homogeneous

than the Li. Same can be demonstrated by selecting extreme areas in the sample and comparing their spectra as shown in Figure S25 (Supporting Information). All regions in the charged sample show systematically higher oxidation state than discharged sample. Instead, in Li-containing some selections of the discharged sample are more oxidized than others of the charged one.
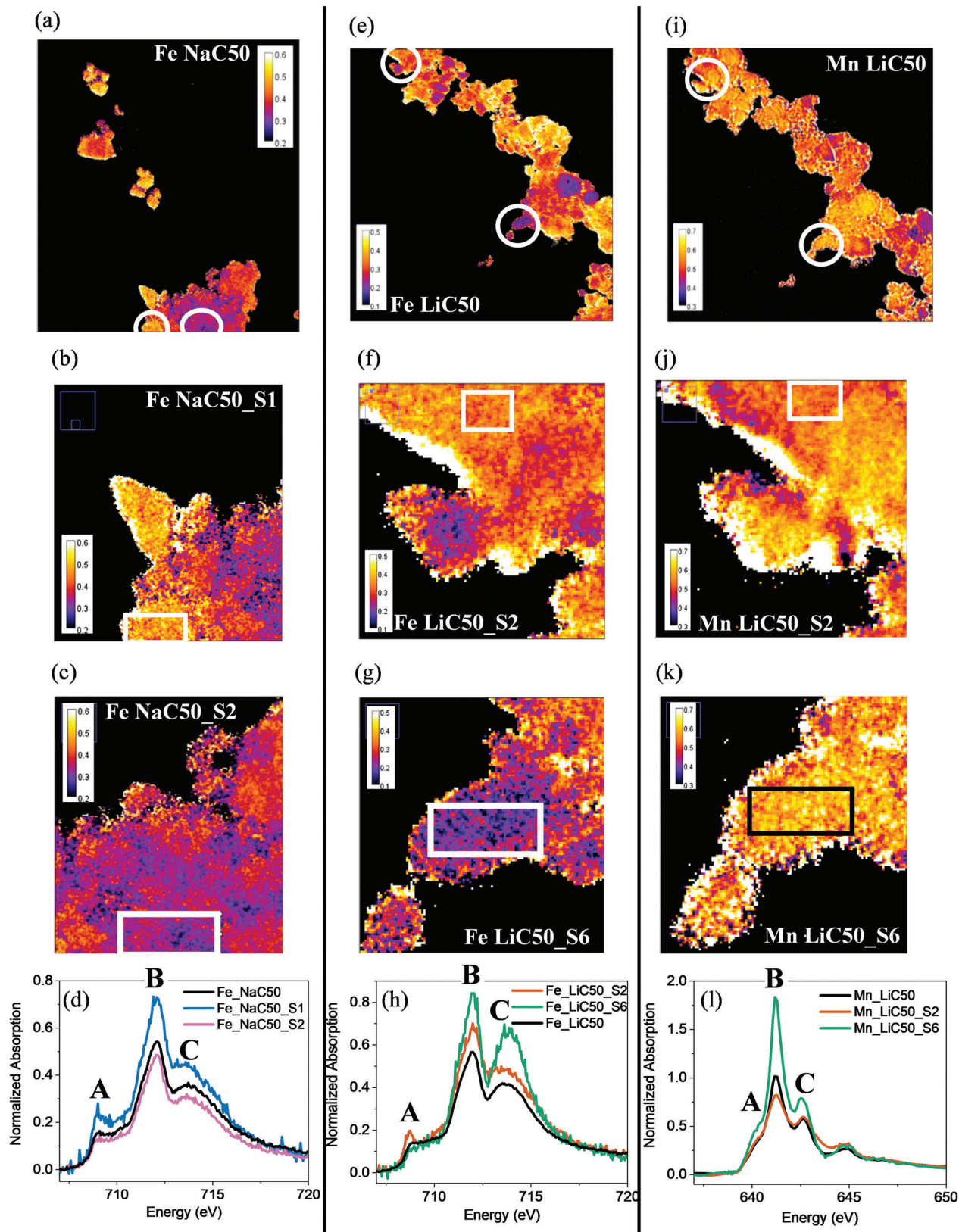
**ADVANCED
SCIENCE NEWS**

www.advancedsciencenews.com

**small
methods**

www.small-methods.com

Figure 5. Chemical state maps of full images and manual selections with their corresponding spectra: Fe_NaC50 (a), more oxidized Fe_NaC50_S1 (b), more reduced Fe_NaC50_S2 (c), their spectra (d), Fe_LiC50 (e), more oxidized Fe_LiC50_S2 (f), more reduced Fe_LiC50_S6 (g), their spectra (h), Mn_LiC50 (i), transferred selections from Fe to Mn edge – more oxidized Mn_LiC50_S2 (j), more reduced Mn_LiC50_S6 (k), and their spectra (l).

**ADVANCED
SCIENCE NEWS**

www.advancedsciencenews.com

**small
methods**

www.small-methods.com
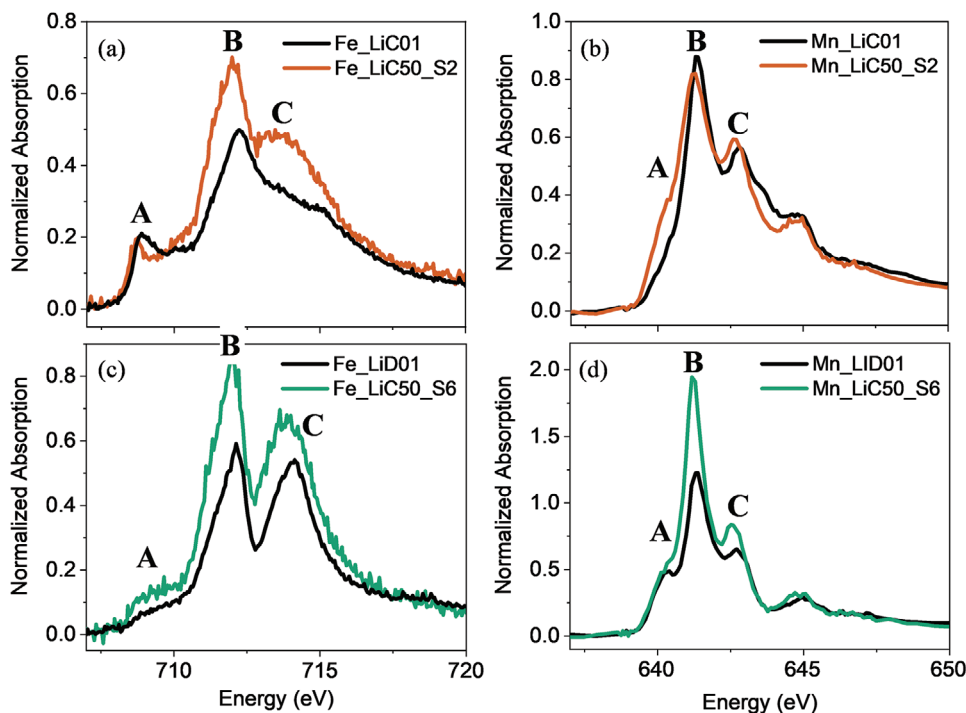
Figure 6. Spectra of the "oxidized selection" of a) Fe_LiC50_S2 versus Fe_LiC01, b) Mn_LiC50_S2 versus Mn_LiC01, and "reduced selection" of c) Fe_LiC50_S6 versus Fe_LiD01 and d) Mn_LiC50 versus Mn_LiD01_S6.

3. Conclusion

The research results enable a deeper understanding of the MnHCF aging process, highlighting the advantages of its use as cathode material for the sodium-ion system, as it is more stable toward the formation of the heterogeneities inside its structure than the lithium one. Charge state inhomogeneities are more evident at the Fe L-edge, compared to Mn L-edge, although the results are well-correlated to each other. It is significant that precisely Fe does not show strong variation by

XAS in the hard X-ray range, hence showing the complementarity of those two techniques. By using the soft x-rays, it is also possible to probe the N K-edge. Although not providing remarkable additional information, the average spectra of N K-edge show small modification that can be related to the electronic changes inferred from L-edge spectra of transition metals. This indicates an electron delocalization that affects the whole framework. This information confirms that soft-TXM can be a valuable characterization technique in battery applications.
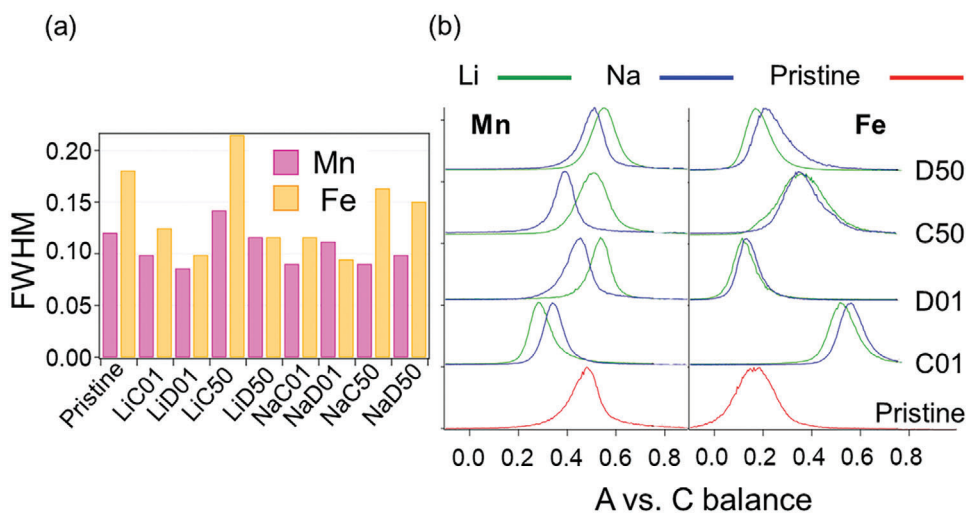

Figure 7. The comparison of a) FWHM of histograms for the entire set of samples, and b) stacked histograms for the whole set of samples of Mn and Fe L-edge spectra, where A versus C balance corresponds to arctangent ratio between peak A and C.

2300718 (9 of 11)

4. Experimental Section

Synthesis: Na-rich MnHCF was synthesized through a simple and scalable co-precipitation method.[28] The reagents manganese sulphate monohydrate ($MnSO_4 \cdot H_2O$), sodium ferrocyanide decahydrate ($Na_4[Fe(CN)_6] \cdot 10H_2O$) and sodium sulphate ($Na_2SO_4$) were used without further purification (Sigma Aldrich). Aqueous solutions of $MnSO_4 \cdot H_2O$ and $Na_4[Fe(CN)_6] \cdot 10H_2O$ were added dropwise to an aqueous solution of Na_2SO_4 (0.1 L, of each 0.1000 M solution) by means of a peristaltic pump at a rate of 3.8 mL min^{-1} upon continuous stirring and constant temperature (40 ± 2 °C regulating with a thermostated bath). The obtained solution was aged for 5 days. After centrifugation, the solid fraction was washed three times with distilled water, dried at 60 °C for 48 h and grinded in an agate mortar. The formula of the synthesized material was $Na_{1.9}Mn_{1.1}[Fe(CN)_6] \cdot 2.1H_2O$, obtained by inductively coupled plasma optical emission spectroscopy with Spectro Arcos FHS12 instrument, and TGA with TA Discovery TGA instrument (before vacuum drying of the material).

Electrode Preparation: The cathode slurry was prepared by mixing 85 wt% of active material (Na-rich MnHCF), 10 wt% conductive agent (Super C65, IMERYS), and 5 wt% binder (polyvinylidene difluoride; Solef 6020, Solvay Polymer specialties). The binder was at first dissolved in dried N-methyl-2-pyrrolidone (NMP) to obtain a 10 wt% solution. Additional NMP was added to adjust the viscosity of the slurry. The final solid content ratio (m(solid)/m(solid+solvent)) was 0.20. The materials were mixed using a ball-milling procedure, which consisted of two 1 h repetitions with a 10 min break in-between the stages. The slurries were cast on aluminum foil (thickness 20 μm) previously cleaned with ethanol and dried at 80 °C overnight, using a blade coater (blade height of 200 μm). Following coatings were dried at 60 °C overnight. Disk electrodes with a diameter of 12 mm were cut using a Hohsen puncher. The MnHCF electrodes were weighed and then pressed at 10 tons for 10 s. The final electrodes were dried at 120 °C under vacuum (10^{-6} bar) for 24 h and stored in an Ar-filled glove box. The mass loading of the electrodes was 2.04±0.09 mg$_{MnHCF}$ cm^{-2}, while the electrode thickness, measured after the final drying process using a Mitutoyo C112XBS micrometer with precision of 1 μm, was in the range of 19 ± 2 μm.

Cell assembly was conducted in Ar-filled glove boxes (MBRAUN MB 200B ECO) with oxygen and water contents lower than 0.1 ppm. The MnHCF electrodes were used as positive electrodes in the three-electrode Swagelok cells, employing GF/A Whatman paper as a separator and Li or Na metal foils as the counter and the reference electrodes. As the electrolyte, LP30 (1.0 M LiPF$_6$ dissolved in the 1:1 volumetric mixture of ethylene carbonate and dimethyl carbonate (EC/DMC = 50/50 v/v)) was employed in Li-cells and 1 M NaPF$_6$ in propylene carbonate (PC) in Na-cells. Galvanostatic cycling with potential limitation in constant current mode was performed on a battery cycler (Maccor, Series 4000) at a rate of C/10. Considering a theoretical specific capacity of 151.5 mAh g^{-1}, imposed current was ≈0.035 mA. Cycling was performed in the 2.3 < E < 4.3 V versus Li$^+$/Li or in the 2.0 < E < 4.0 V versus Na$^+$/Na starting at open circuit potential with a positive initial polarization after 6 h of rest time. All tests were performed in climatic chambers at a temperature of 20 ± 2 °C.

TXM Measurements and Analysis: To prevent any moisture contamination of the samples, cells were disassembled after cycling in Ar-filled gloveboxes. Electrodes were removed and rinsed with DMC (Li-ion cells) or PC (Na-ion cells), sandwiched between two polypropylene sheets and sealed under vacuum for shipping to the ALBA light source. The bags were opened in glove box, the electrodes scraped with a blade and deposited on a carbon-coated TEM Au grid, which were then placed on TXM holders and transferred to the microscope chamber of the MISTRAL beamline[50] by a transfer system avoiding any atmospheric contamination.

Analysis of transmission soft X-ray microscopy was performed on MnHCF samples (Table S1, Supporting Information) at the Mn and Fe L-edges as well as at the K-edge of N.

Image Treatment: For the statistical overview of the spectromicroscopy measurements and better recognition of chemical heterogeneities, the methodology mainly followed a previously proposed procedure.[32] Briefly, for each sample and for every edge 30 images were averaged around each observed peak maximum. Sample pixels were isolated by setting to NaN those, where the standard deviation was larger than the average at the maximum intensity (further details in Supporting Information). Each of these average images was then transformed into 1D arrays, which were then plotted against each other to obtain what called "phase maps". Provided that absorbance was linear with the thickness, if only one composition was present with the variable thickness, all points would ideally align on a straight line that would intersect the origin. In practice, the result was a spread cloud due to spectral noise and composition fluctuations. To reduce distortions, the points distributions versus direction were represented as function of the angle rather than versus the xy ratio. Thus, the spatial distribution of the relative intensity of a Peak A versus Peak C was represented as map of arctan(Peak A/Peak C), where each peak was the intensity difference between peak maximum and background, as shown in Figure S6a (Supporting Information).

After obtaining such maps highlighting chemical heterogeneity, manual selection of different homogeneous regions was performed using the ImageJ software,[51] allowing to extract the spectrum averaged over a given selection of the field of view. Specific regions were first chosen from the Fe L-edge measures and then also selected in the Mn-edge ones for comparison (Figures S7-S24, Supporting Information).

Supporting Information

Supporting Information is available from the Wiley Online Library or from the author.

Conflict of Interest

The authors declare no financial conflict of interest.

Data Availability Statement

The data that support the findings of this study are available from the corresponding author upon reasonable request.

[1] L. Lu, X. Han, J. Li, J. Hua, M. Ouyang, *J. Power Sources* **2013**, *226*, 272.

[2] H. S. Hirsh, Y. Li, D. H. S. Tan, M. Zhang, E. Zhao, Y. S. Meng, *Adv. Energy Mater.* **2020**, *10*, 2001274.

[3] J. Y. Hwang, S. T. Myung, Y. K. Sun, *Chem. Soc. Rev.* **2017**, *46*, 3529.

[4] M. D. Slater, D. Kim, E. Lee, C. S. Johnson, *Adv. Funct. Mater.* **2013**, *23*, 947.

[5] D. I. Iermakova, R. Dugas, M. R. Palacín, A. Ponrouch, *J. Electrochem. Soc.* **2015**, *162*, A7060.

[6] J. Song, B. Xiao, Y. Lin, K. Xu, X. Li, *Adv. Energy Mater.* **2018**, *8*, 1703082.

[7] E. Matios, H. Wang, C. Wang, W. Li, *Ind. Eng. Chem. Res.* **2019**, *58*, 9758.

[8] B. Sayahpour, H. Hirsh, S. Parab, L. H. B. Nguyen, M. Zhang, Y. S. Meng, *MRS Energy Sustain.* **2022**, *9*, 183.

[9] J. M. Tarascon, M. Armand, *Nature* **2001**, *414*, 359.

[10] G. H. Newman, L. P. Klemann, *J. Electrochem. Soc.* **1980**, *127*, 2097.

[11] C. Delmas, C. Fouassier, P. Hagenmuller, *Physica. B+C* **1980**, *99*, 81.

[12] G. Ali, J. H. Lee, D. Susanto, S. W. Choi, B. W. Cho, K. W. Nam, K. Y. Chung, *ACS Appl. Mater. Interfaces* **2016**, *8*, 15422.

[13] K. Trad, D. Carlier, L. Croguennec, A. Wattiaux, M. ben Amara, C. Delmas, *Chem. Mater.* **2010**, *22*, 5554.

[14] A. Daidouh, C. Durio, C. Pico, M. L. Veiga, N. Chouaibi, A. Ouassini, *Solid State Sci.* **2002**, *4*, 541.

[15] E. Boivin, J. N. Chotard, T. Bamine, D. Carlier, P. Serras, V. Palomares, T. Rojo, A. Iadecola, L. Dupont, L. Bourgeois, F. Fauth, C. Masquelier, L. Croguennec, *J. Mater. Chem. A* **2017**, *5*, 25044.

[16] A. A. Tsirlin, R. Nath, A. M. Abakumov, Y. Furukawa, D. C. Johnston, M. Hemmida, H. A. Krug von Nidda, A. Loidl, C. Geibel, H. Rosner, *Phys. Rev. B* **2011**, *84*, 014429.

[17] W. Massa, O. V. Yakubovich, O. V. Dimitrova, *Solid State Sci.* **2002**, *4*, 495.

[18] J. M. le Meins, M. P. Crosnier-Lopez, A. Hemon-Ribaud, G. Courbion, *J. Solid State Chem.* **1999**, *148*, 260.

[19] J. B. Goodenough, H. Y. P. Hong, J. A. Kafalas, *Mater. Res. Bull.* **1976**, *11*, 203.

[20] A. Manthiram, J. B. Goodenough, *J. Power Sources* **1989**, *26*, 403.

[21] Y. Lu, L. Wang, J. Cheng, J. B. Goodenough, *ChemComm* **2012**, *48*, 6544.

[22] L. Wang, Y. Lu, J. Liu, M. Xu, J. Cheng, D. Zhang, J. B. Goodenough, *Angew. Chem., Int. Ed.* **2013**, *52*, 1964.

[23] Contemporary Amperex Technology Co., Limited, CATL Unveils Its Latest Breakthrough Technology by Releasing Its First Generation of Sodium-ion Batteries, https://www.catl.com/en/news/665.html (accessed: May 2023).

[24] Altris AB, Technology: Prussian White, https://www.altris.se/technology/ (accessed: May 2023).

[25] Natron Energy, Inc. Natron's Prussian Blue Sodium-ion technology, https://natron.energy/technology/ (accessed: May 2023).

[26] J. Qian, C. Wu, Y. Cao, Z. Ma, Y. Huang, X. Ai, H. Yang, *Adv. Energy Mater.* **2018**, *8*, 1702619.

[27] Y. You, X. L. Wu, Y. X. Yin, Y. G. Guo, *J. Mater. Chem. A* **2013**, *1*, 14061.

[28] A. Mullaliu, J. Asenbauer, G. Aquilanti, S. Passerini, M. Giorgetti, *Small Methods* **2019**, *4*, 1900529.

[29] C. Gao, Y. Lei, Y. Wei, H. Wang, F. Yuan, F. Kang, D. Zhai, *Chem. Eng. J.* **2022**, *431*, 133926.

[30] C. Tian, Y. Xu, D. Nordlund, F. Lin, J. Liu, Z. Sun, Y. Liu, M. Doeff, *Joule* **2018**, *2*, 464.

[31] A. Mullaliu, M. Gaboardi, J. R. Plaisier, S. Passerini, M. Giorgetti, *ACS Appl. Energy Mater.* **2020**, *3*, 5728.

[32] A. Sorrentino, L. Simonelli, A. Kazzazi, N. Laszczynski, A. Birrozzi, A. Mullaliu, E. Pereiro, S. Passerini, M. Giorgetti, D. Tonti, *Appl. Sci.* **2021**, *11*, 2791.

[33] J. Maser, *Microsc. Microanal.* **2001**, *7*, 536.

[34] M. L. Baker, M. Mara, J. Yan, K. Hodgson, B. Hedman, E. Solomon, *Coord. Chem. Rev.* **2017**, *345*, 182.

[35] A. Mullaliu, G. Aquilanti, P. Conti, M. Giorgetti, S. Passerini, *ChemSusChem* **2020**, *13*, 608.

[36] J. Song, L. Wang, Y. Lu, J. Liu, B. Guo, P. Xiao, J. J. Lee, X. Q. Yang, G. Henkelman, J. B. Goodenough, *J. Am. Chem. Soc.* **2015**, *137*, 2658.

[37] M. Pasta, R. Y. Wang, R. Ruffo, R. Qiao, H. W. Lee, B. Shyam, M. Guo, Y. Wang, L. A. Wray, W. Yang, M. F. Toney, Y. Cui, *J. Mater. Chem. A* **2016**, *4*, 4211.

[38] D. Asakura, E. Hosono, Y. Nanba, H. Zhou, J. Okabayashi, C. Ban, P. A. Glans, J. Guo, T. Mizokawa, G. Chen, A. J. Achkar, D. G. Hawthron, T. Z. Regier, H. Wadati, *AIP Adv.* **2016**, *6*, 035105.

[39] M. A. Arrio, P. Sainctavit, C. Cartier dit Moulin, T. Mallah, M. Verdaguer, E. Pellegrin, C. T. Chen, *J. Am. Chem. Soc.* **1996**, *118*, 6422.

[40] R. K. Hocking, E. C. Wasinger, F. M. F. de Groot, K. O. Hodgson, B. Hedman, E. I. Solomon, *J. Am. Chem. Soc.* **2006**, *128*, 10442.

[41] D. Asakura, M. Okubo, Y. Mizuno, T. Kudo, H. Zhou, K. Amemiya, F. M. F. de Groot, J. L. Chen, W. C. Wang, P. A. Glans, C. Chang, J. Guo, I. Honma, *Phys. Rev. B* **2011**, *84*, 045117.

[42] T. Yokoyama, T. Tokoro, S. Ohkoshi, K. Hashimoto, K. Okamoto, T. Ohta, *Phys. Rev. B* **2002**, *66*, 184111.

[43] H. Tokoro, S. Miyashita, K. Hashimoto, S. Ohkoshi, *Phys. Rev. B* **2006**, *73*, 172415.

[44] H. Tokoro, S. Ohkoshi, K. Hashimoto, *Appl. Phys. Lett.* **2003**, *82*, 1245.

[45] M. Parthey, M. Kaupp, *Chem. Soc. Rev.* **2014**, *43*, 5067.

[46] R. Qiao, T. Chin, S. J. Harris, S. Yan, W. Yang, *Curr. Appl. Phys.* **2013**, *13*, 544.

[47] L. F. J. Piper, N. F. Quackenbush, S. Sallis, D. O. Scanlon, G. W. Watson, K. W. Nam, X. Q. Yang, K. E. Smith, F. Omenya, N. A. Chernova, M. S. Whittingham, *J. Phys. Chem. C* **2013**, *117*, 10383.

[48] A. Firouzi, R. Qiao, S. Motallebi, C. W. Valencia, H. S. Israel, M. Fujimoto, L. A. Wray, Y. D. Chuang, W. Yang, C. D. Wessells, *Nat. Commun.* **2018**, *9*, 861.

[49] W. Gent, Y. Li, S. Ahn, J. Lim, Y. Liu, A. M. Wise, C. B. Gopal, D. N. Mueller, R. Davis, J. N. Weker, J. H. Park, S. K. Doo, W. C. Chueh, *Adv. Mater.* **2016**, *28*, 6631.

[50] A. Sorrentino, J. Nicolas, R. Valcárcel-Fernández, F. J. Chichón, M. Rosanes, J. Avila, A. Tkachuk, J. Irwin, S. Ferrer, E. Pereiro, *J. Synchrotron Radiat.* **2015**, *22*, 1112.

[51] C. A. Schneider, W. S. Rasband, K. W. Eliceiri, *Nat. Methods* **2012**, *9*, 671.